

The cosmic 21-cm revolution: charting the first billion years of our Universe

Andrei Mesinger

July 26, 2019

Contents

1	Observational strategies: power spectra and images	1
1.1	Chapter layout	1
1.2	Interferometry overview	2
1.3	21 cm observables: power spectra and images	4
1.4	Interferometric calibration and 21 cm observations	5
1.4.1	Redundant calibration	7
1.5	Array design	7
2	Future prospects	10
2.1	Forthcoming interferometric ground based instruments and upgrades	10
2.1.1	The Hydrogen Epoch of Reionization Array	10
2.1.2	The Large aperture Experiment to detect the Dark Ages	11
2.2	A Section	11

Preface

This set of files can be used to create your typescript in \LaTeX . You can add packages as necessary.

Remember that references need to be at the chapter level and you may find the package `chapterbib` useful for this.

About the Author



Remember to include a brief biography of the Authors or Editors, including a photo.

Contributors

Gianni Bernardi

INAF - Istituto di Radio Astronomia
via Gobetti 101, 40129, Bologna, Italy &
Department of Physics and Electronics
Rhodes University
PO Box 94, Grahamstown, 6140, South Africa

Bradley Greig

School of Physics
The University of Melbourne
Parkville, Melbourne VIC, Australia

Vibor Jelić

Ruđer Bošković Institute
Zagreb, Croatia

Peter Jones

Department of Physics
University of New England
Acadia, Maine, USA

Jonathan Pritchard

Blackett Laboratory
Imperial College
London, UK

Simon Smith

Department of Electrical Engineering
University of Oxford, Oxford, UK

Cathryn M. Trott

International Centre for Radio Astronomy Research
Curtin University, Bentley WA, Australia

Chapter 1

Observational strategies: power spectra and images

Gianni Bernardi (INAF-IRA & Rhodes University)

Abstract

This chapter reviews the basics of radio interferometry (van-Citter-Zernike theorem, uv -coverage, image formation calibration) and how they are linked to the measurements of the 21-cm power spectrum and its tomography

1.1 Chapter layout

- review of basics of interferometry: van-Citter-Zernike theorem, uv -coverage, image formation;
- from visibilities to power spectra (in particular the delay transform approach - some overlap with Trott's chapter);
- interferometric calibration: impact on foreground subtraction, calibration errors redundant calibration;
- array design: power spectrum vs imaging, minimum vs maximum redundancy - some overlap with Trott's chapter?;
- impact of calibration errors on power spectra;
- ionospheric impact/calibration;
- 21-cm image tomography;

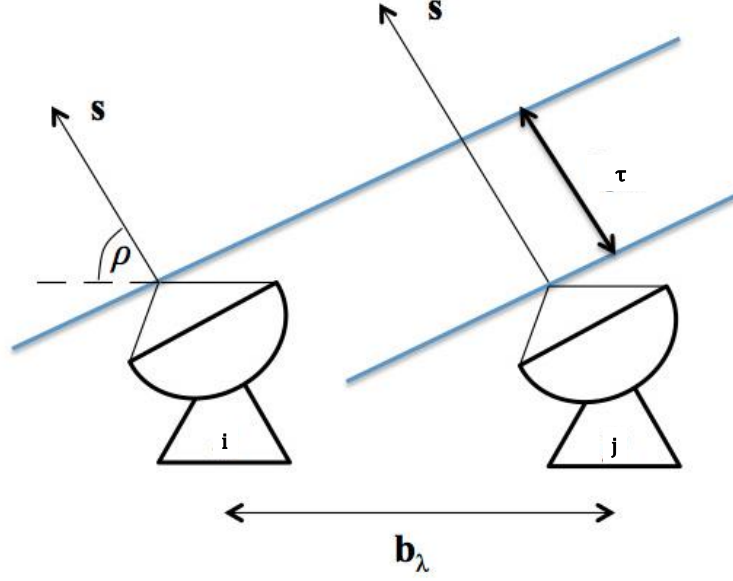


Figure 1.1: A standard schematic of the two element interferometer.

1.2 Interferometry overview

The Van Cittert-Zernike theorem expresses the fundamental relationship between the sky spatial brightness (or brightness distribution) I and the quantity measured by an interferometer, i.e. the visibility V (e.g., [18]):

$$V_{ij}(\mathbf{b}, \lambda) = \int_{\Omega} \bar{I}(\hat{\sigma}, \lambda) e^{-2\pi i \mathbf{b} \cdot \hat{\sigma}} d\sigma, \quad (1.1)$$

where \mathbf{b} is the baseline vector that separates between antenna i and j and $\hat{\sigma}$ is the observing direction (see Figure 1.2). The baseline vector is here specified in wavelengths, i.e. $\mathbf{b} = \frac{\mathbf{b}_m}{\lambda}$, where \mathbf{b}_m is the baseline vector expressed in meters and λ is the observing wavelength. The celestial signal travels an extra path between antenna i and j that correspond to a geometrical time delay $\tau = \mathbf{b} \cdot \hat{\sigma}$, where the word “geometrical” refers to the fact that the delay depends upon the source position in the sky and the relative separation between the two antennas. The sky brightness distribution does not enter directly in equation 1.1, but filtered by the antenna primary beam response A that depends upon the direction in the sky and the wavelength, i.e. $\bar{I} = AI$. The response of the primary beam attenuates the sky emission away from the pointing direction, effectively reducing the field of view θ of the instrument. Generally speaking, the size of the field of view is essentially given by the antenna diameter D :

$$\theta \approx \frac{\lambda}{D}. \quad (1.2)$$

The integral of equation 1.1 is taken over the source size Ω . Equation 1.1 is often re-written in a different coordinate system, i.e. the components of the baseline vector (u, v, w) and

the reciprocal (l, m, n) , where (l, m) are the coordinates in the plane on the sky tangent to the observing direction n (for a detailed discussion on coordinate systems see, for example [18]). Using this different coordinate system, equation 1.1 becomes (e.g., [18]):

$$V_{ij}(u, v, w, \lambda) = \int_{\Omega} \bar{I}(l, m, \lambda) e^{-2\pi i(ul+vm+wn)} \frac{dl dm dn}{\sqrt{1-l^2-m^2}}, \quad (1.3)$$

Although low frequency radio observations are intrinsically wide-field, for the purpose of studying the 21 cm observables, we can reduce equation 1.3 to a two dimensional Fourier transform:

$$V_{ij}(u, v, \lambda) = \int_{\Omega} \bar{I}(l, m, \lambda) e^{-2\pi i(ul+vm)} dl dm. \quad (1.4)$$

Equation 1.4 indicates that an *interferometer measures the two dimensional Fourier transform of the spatial sky brightness distribution*. If our goal is to reconstruct the sky brightness distribution, equation 1.4 can be inverted into its corresponding Fourier pair:

$$\bar{I}(l, m, \lambda) = \int_{-\infty}^{+\infty} V_{ij}(u, v, \lambda) e^{2\pi i(ul+vm)} du dv. \quad (1.5)$$

Equation 1.5 is, however, a poor reconstruction of the sky brightness distribution as only one Fourier mode is sampled at the time t . Strictly speaking, indeed, all the quantities in equation 1.4 and 1.5 are time variable. In most cases, the time dependence of the primary beam and the sky brightness distribution can be neglected, however, this is not the case for the visibility V as the projection of the baseline vector with respect to the source direction changes significantly throughout a long (e.g. a few hours) track. In this way, many measurements of the visibility coherence function V as $(u, v,)$ change with time can be made, allowing for a better reconstruction of the $\bar{I}(l, m, \lambda)$ function. This method is commonly described as *filling the uv plane via Earth rotation synthesis* and was invented by [12]. The other (complementary) way to fill the uv plane is to deploy more antennas on the ground in order to increase the number of instantaneous measurements of independent Fourier modes. If N antennas are connected in an interferometric array, $\frac{N(N-1)}{2}$ instantaneous measurements are made.

The combination of a large number of antennas and the Earth rotation synthesis, defines the sampling function $S(u, v,)$ in the uv plane. In any real case, equation 1.5 can therefore be re-written as:

$$\bar{I}_D(l, m, \lambda) = \int_{-\infty}^{+\infty} S(u, v,) V(u, v, \lambda) e^{2\pi i(ul+vm)} du dv \quad (1.6)$$

where \bar{I}_D indicates the sky brightness distribution sampled at a finite number of (u, v) points (often termed *dirty image*) and I dropped the explicit dependence on the antenna pair as redundant at this point. Using the convolution theorem, equation 1.7 can be re-written as:

$$\bar{I}_D(l, m, \lambda) = \tilde{S}\tilde{V} = \tilde{S} * \tilde{V} = \text{PSF}(l, m, \lambda) * \tilde{V}(l, m, \lambda), \quad (1.7)$$

where the tilde indicates the Fourier transform, $*$ the convolution operation and PSF is the Point Spread Function, i.e. the response of the interferometric array to a point sources which, in our case, is also the Fourier transform of the uv coverage.

I will give some examples of sampling functions for different instruments in Section 1.5, however, the sampling function always effectively reduces the integral over a finite (often not contiguous) area of the uv plane. In particular, the sampled uv plane is restricted to a minimum uv distance that cannot be shorter than the antenna size and a maximum uv distance given by equation 1.2. The result of not sampling all the Fourier modes is that the PSF has got “sidelobes”, i.e. nulls and secondary lobes that can often contaminate fainter true sky emission. The best reconstruction of the sky brightness distribution \bar{I} requires deconvolution of the dirty image from the PSF.

1.3 21 cm observables: power spectra and images

The ultimate goal of 21 cm observations is to image the spatial distribution of the 21 cm signal as a function of redshift, also known as *21 cm tomography*. Given the current theoretical predictions, such observations need to achieve mK sensitivity on a few arcminute angular scales (see Chapter 1 in this book). Most of the current arrays, however, only have the sensitivity to perform a statistical detection of the 21 cm, i.e. to measure its power spectrum. Given an intensity field T function of the three dimensional spatial coordinate \mathbf{x} , its power spectrum $P(k)$ can be defined as:

$$\langle \tilde{T}^*(\mathbf{k}) \tilde{T}(\mathbf{k}') \rangle = (2\pi)^3 P(k) \delta^3(\mathbf{k} - \mathbf{k}') \quad (1.8)$$

where $\langle \rangle$ indicates the ensemble average, \mathbf{k} is the Fourier conjugate of \mathbf{x} , tilde the Fourier transform, $*$ the complex conjugate operator and δ the Dirac delta function. In 21 cm observations, power spectra can be computed directly from interferometric image cubes after deconvolution of $\bar{I}_D(l, m, \lambda)$ from the point spread function (e.g., [11], [5], [1], [9]). An alternative way to estimate the 21 cm power spectrum that has driven the design and calibration strategies of some of the arrays. Equation 1.4 already shows that the interferometer is a “natural” spatial power spectrum instrument (e.g., [19]). Visibilities can be further Fourier transformed along the frequency axis (the so-called *delay transform*, [8]):

$$\tilde{V}_{ij}(u, v, \tau) = \int_B \bar{I}(l, m, \nu) e^{-2\pi i \nu \tau} d\nu \quad (1.9)$$

where B is the observing bandwidth and τ is the geometrical delay. The delay transform is therefore proportional to the three dimensional power spectrum ([7]):

$$P(k) \propto \tilde{V}_{ij}(|\mathbf{b}|, \tau), \quad (1.10)$$

where the proportionality constant transforms the visibility units into power units ([7]) and the observer units (\mathbf{b}, τ) map directly in k modes parallel and perpendicular to the line of sight (e.g., [?]):

$$k_{\perp} = \frac{2\pi|\mathbf{b}|}{D} = \frac{2\pi\sqrt{u^2 + v^2}}{D}, \quad k_{\parallel} = \frac{2\pi f_{21} H_0 E(z)}{c * 1_z)^2} \tau, \quad (1.11)$$

where D is the transverse comoving distance, $f_{21} = 1421$ MHz, H_0 is the Hubble constant and $E(z) = \sqrt{\Omega_m(1+z)^3 + \Omega_k(1+z)^2 + \Omega_{\Lambda}}$. Due to the dependence of the geometrical delay

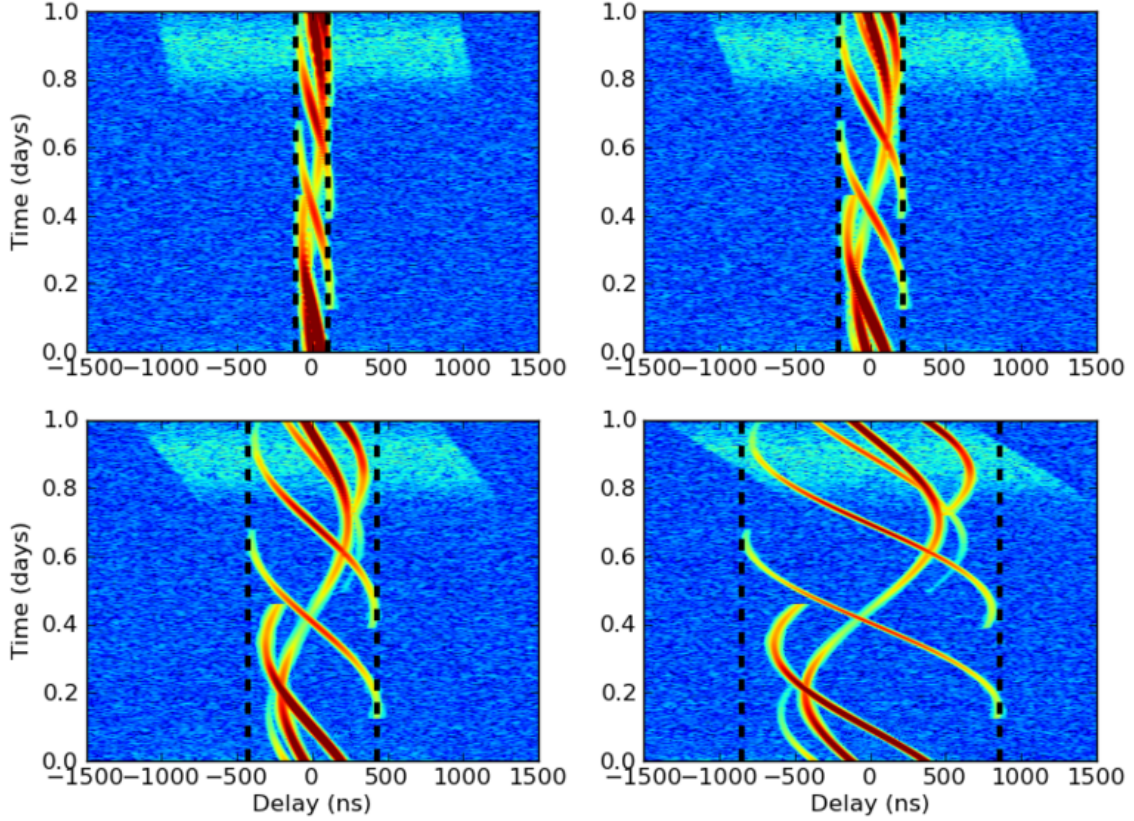


Figure 1.2: A standard schematic of the two element interferometer.

upon frequency, equation 1.10 is only valid for short baselines, typically shorter than a few hundred meters, for which the geometrical delay is fairly constant across the bandwidth and lines of constant k_{\parallel} are practically orthogonal to the k_{\perp} axis ([7].

Equation 1.9 does not only provide a link between visibilities and three dimensional power spectra, but also introduces the concept of “horizon limit” which is the maximum delay allowed

The power spectrum has a very close connection with the visibility measured by an interferometer (include CMB references). A direct relationship between the three dimensional 21 cm distribution and interferometric visibilities can be derived. An interferometric array already operates a two dimensional Fourier transform of the sky brightness distribution, therefore a Fourier transform

1.4 Interferometric calibration and 21 cm observations

Celestial signals always experience a corruption due to the non-ideal instrumental response that needs to be corrected for a posteriori, in a process that is known as interferometric calibration. Calibration relies on the definition of a data model where the corruptions are de-

scribed by antenna based quantities known as Jones matrices. The data model is known as the interferometric measurement equation ([4],[14]) that will be summarized in the following.

If antenna 1 and antenna 2 measure two orthogonal, linear polarizations x and y , the cross-polarization visibility products can be grouped in a 2×2 matrix \mathbf{V}

$$\mathbf{V}^{12}(u, v, \lambda) \equiv \begin{bmatrix} V_{xx}^{12}(u, v, \lambda) & V_{xy}^{12}(u, v, \lambda) \\ V_{yx}^{12}(u, v, \lambda) & V_{yy}^{12}(u, v, \lambda) \end{bmatrix}. \quad (1.12)$$

The sky brightness distribution I can also be written as a 2×2 matrix \mathbf{B} using the Stokes parameters as a polarization basis:

$$\mathbf{B}_I(l, m, \lambda) \equiv \begin{bmatrix} I(l, m, \lambda) + Q(l, m, \lambda) & U(l, m, \lambda) + iV(l, m, \lambda) \\ U(l, m, \lambda) - iV(l, m, \lambda) & I(l, m, \lambda) - Q(l, m, \lambda) \end{bmatrix}. \quad (1.13)$$

At this point, equation 1.3 can be written by including the corruptions represented by the Jones matrices J ([4],[14]):

$$\mathbf{V}^{12}(u, v, \lambda) = \mathbf{J}^1 \left(\int_{\Omega} \mathbf{B}_I(l, m, \lambda) e^{-2\pi i(ul+vm)} dl dm \right) (\mathbf{J}^2)^H \quad (1.14)$$

Equation 1.14 is known as the measurement equation and is the core of interferometric calibration. For an array with N antennas, equation 1.14 can be written for each of the $\frac{N(N-1)}{2}$ visibilities forming an overdetermined system of equations. The development of calibration algorithms is a very active research line ([6], [17], [16]) although beyond the scope of this chapter and we mention it here for completeness. The solution of the system of calibration equations requires some knowledge of the sky brightness distribution \mathbf{B}_I , or a *sky model*. Traditionally this is achieved by observing a calibration source, i.e. a bright, unresolved point source with known spectral and polarization properties. Calibration solutions are then applied to the observed field that, in turn, is then used to improve the sky model \mathbf{B}_I which, in turn, leads to more accurate calibration solutions J in the loop that is traditionally called *self calibration* ([3], [10]). This approach can lead to a high accurate calibration (e.g., [2], [15]).

The advantage of the measurement equation is that it can factorize different physical terms into different matrices. For example, the frequency response of the electronic filters and its time variations essentially affects only the two polarization response and are modeled with a diagonal Jones matrix B :

$$\mathbf{B}(t, \lambda) \equiv \begin{bmatrix} b_x(t, \lambda) & 0 \\ 0 & b_y(t, \lambda) \end{bmatrix}, \quad (1.15)$$

whereas the undesired instrumental leakage between the two orthogonal polarized is represented by a D Jones matrix of the form:

$$\mathbf{D}(t, \lambda) \equiv \begin{bmatrix} 1 & d_x(t, \lambda) \\ -d_y(t, \lambda) & 1 \end{bmatrix}, \quad (1.16)$$

and the measurement equation can be written as:

$$\mathbf{V}^{12}(u, v, \lambda) = \mathbf{B}^1 \mathbf{D}^1 \left(\int_{\Omega} \mathbf{B}_I(l, m, \lambda) e^{-2\pi i(ul+vm)} dl dm \right) (\mathbf{D}^2)^H (\mathbf{B}^2)^H. \quad (1.17)$$

Retaining only the first order terms, equation 1.17 can be written as ([13]):

$$V_{xx}^{12}(u, v, \lambda) = b_x^1 b_x^{2,*} [I(l, m, \lambda) - Q(l, m, \lambda)] \quad (1.18)$$

$$V_{xy}^{12}(u, v, \lambda) = b_x^1 b_y^{2,*} [(d_x^1 - d_y^{2,*})I(l, m, \lambda) + U(l, m, \lambda) + iV(l, m, \lambda)] \quad (1.19)$$

$$V_{yx}^{12}(u, v, \lambda) = b_y^1 b_x^{2,*} [(d_x^2 - d_y^{1,*})I(l, m, \lambda) + U(l, m, \lambda) - iV(l, m, \lambda)] \quad (1.20)$$

$$V_{yy}^{12}(u, v, \lambda) = b_y^1 b_y^{2,*} [I(l, m, \lambda) - Q(l, m, \lambda)] \quad (1.21)$$

This simplified version of the measurement equation offers an intuitive understanding as to why calibration is so important in 21 cm observations.

The separation of the cosmological signal from the much brighter foreground emission is the key challenge in interferometric observations of the 21 cm signal. As long as foreground emission is smooth in frequency the separation of the 21 cm signal is possible. However, it has been realized already in the early days that there is a strong coupling between foregrounds and interferometric calibration.

1.4.1 Redundant calibration

1.5 Array design

Bibliography

- [1] A. P. Beardsley, B. J. Hazelton, I. S. Sullivan, P. Carroll, N. Barry, M. Rahimi, B. Pindor, C. M. Trott, J. Line, D. C. Jacobs, M. F. Morales, J. C. Pober, G. Bernardi, J. D. Bowman, M. P. Busch, F. Briggs, R. J. Cappallo, B. E. Corey, A. de Oliveira-Costa, J. S. Dillon, D. Emrich, A. Ewall-Wice, L. Feng, B. M. Gaensler, R. Goeke, L. J. Greenhill, J. N. Hewitt, N. Hurley-Walker, M. Johnston-Hollitt, D. L. Kaplan, J. C. Kasper, H. S. Kim, E. Kratzenberg, E. Lenc, A. Loeb, C. J. Lonsdale, M. J. Lynch, B. McKinley, S. R. McWhirter, D. A. Mitchell, E. Morgan, A. R. Neben, N. Thyagarajan, D. Oberoi, A. R. Offringa, S. M. Ord, S. Paul, T. Prabu, P. Procopio, J. Riding, A. E. E. Rogers, A. Rosh, N. Udaya Shankar, S. K. Sethi, K. S. Srivani, R. Subrahmanyam, M. Tegmark, S. J. Tingay, M. Waterson, R. B. Wayth, R. L. Webster, A. R. Whitney, A. Williams, C. L. Williams, C. Wu, and J. S. B. Wyithe. First Season MWA EoR Power spectrum Results at Redshift 7. *ApJ*, 833:102, December 2016.
- [2] G. Bernardi, A. G. de Bruyn, G. Harker, M. A. Brentjens, B. Ciardi, V. Jelić, L. V. E. Koopmans, P. Labropoulos, A. Offringa, V. N. Pandey, J. Schaye, R. M. Thomas, S. Yatawatta, and S. Zaroubi. Foregrounds for observations of the cosmological 21 cm line. II. Westerbork observations of the fields around 3C 196 and the North Celestial Pole. *A&A*, 522:A67, November 2010.
- [3] T. J. Cornwell and P. N. Wilkinson. A new method for making maps with unstable radio interferometers. *MNRAS*, 196:1067–1086, September 1981.
- [4] J. P. Hamaker, J. D. Bregman, and R. J. Sault. Understanding radio polarimetry. I. Mathematical foundations. *A&AS*, 117:137–147, May 1996.
- [5] G. Harker, S. Zaroubi, G. Bernardi, M. A. Brentjens, A. G. de Bruyn, B. Ciardi, V. Jelić, L. V. E. Koopmans, P. Labropoulos, G. Mellema, A. Offringa, V. N. Pandey, A. H. Pawlik, J. Schaye, R. M. Thomas, and S. Yatawatta. Power spectrum extraction for redshifted 21-cm Epoch of Reionization experiments: the LOFAR case. *MNRAS*, 405:2492–2504, July 2010.
- [6] D. A. Mitchell, L. J. Greenhill, R. B. Wayth, R. J. Sault, C. J. Lonsdale, R. J. Cappallo, M. F. Morales, and S. M. Ord. Real-Time Calibration of the Murchison Widefield Array. *IEEE Journal of Selected Topics in Signal Processing*, 2:707–717, November 2008.

- [7] A. Parsons, J. Pober, M. McQuinn, D. Jacobs, and J. Aguirre. A Sensitivity and Array-configuration Study for Measuring the Power Spectrum of 21 cm Emission from Reionization. *ApJ*, 753:81, July 2012.
- [8] A. R. Parsons, J. C. Pober, J. E. Aguirre, C. L. Carilli, D. C. Jacobs, and D. F. Moore. A Per-baseline, Delay-spectrum Technique for Accessing the 21 cm Cosmic Reionization Signature. *ApJ*, 756:165, September 2012.
- [9] A. H. Patil, S. Yatawatta, L. V. E. Koopmans, A. G. de Bruyn, M. A. Brentjens, S. Zaroubi, K. M. B. Asad, M. Hatef, V. Jelić, M. Mevius, A. R. Offringa, V. N. Pandey, H. Vedantham, F. B. Abdalla, W. N. Brouw, E. Chapman, B. Ciardi, B. K. Gehlot, A. Ghosh, G. Harker, I. T. Iliev, K. Kakiichi, S. Majumdar, G. Mellema, M. B. Silva, J. Schaye, D. Vrbanc, and S. J. Wijnholds. Upper Limits on the 21 cm Epoch of Reionization Power Spectrum from One Night with LOFAR. *ApJ*, 838:65, March 2017.
- [10] T. J. Pearson and A. C. S. Readhead. Image Formation by Self-Calibration in Radio Astronomy. *ARAA*, 22:97–130, 1984.
- [11] U.-L. Pen, T.-C. Chang, C. M. Hirata, J. B. Peterson, J. Roy, Y. Gupta, J. Odegova, and K. Sigurdson. The GMRT EoR experiment: limits on polarized sky brightness at 150 MHz. *MNRAS*, 399:181–194, October 2009.
- [12] M. Ryle and A. Hewish. The synthesis of large radio telescopes. *MNRAS*, 120:220, 1960.
- [13] R. J. Sault, J. P. Hamaker, and J. D. Bregman. Understanding radio polarimetry. II. Instrumental calibration of an interferometer array. *A&AS*, 117:149–159, May 1996.
- [14] O. M. Smirnov. Revisiting the radio interferometer measurement equation. I. A full-sky Jones formalism. *A&A*, 527:A106, March 2011.
- [15] O. M. Smirnov. Revisiting the radio interferometer measurement equation. II. Calibration and direction-dependent effects. *A&A*, 527:A107, March 2011.
- [16] O. M. Smirnov and C. Tasse. Radio interferometric gain calibration as a complex optimization problem. *MNRAS*, 449:2668–2684, May 2015.
- [17] C. Tasse. Nonlinear Kalman filters for calibration in radio interferometry. *A&A*, 566:A127, June 2014.
- [18] A. Richard Thompson, James M. Moran, and Jr. Swenson, George W. *Interferometry and Synthesis in Radio Astronomy, 3rd Edition*. 2017.
- [19] M. White, J. E. Carlstrom, M. Dragovan, and W. L. Holzapfel. Interferometric Observation of Cosmic Microwave Background Anisotropies. *ApJ*, 514:12–24, March 1999.

Chapter 2

Future prospects

Author Name

Abstract

This chapter discusses some important things

2.1 Forthcoming interferometric ground based instruments and upgrades

2.1.1 The Hydrogen Epoch of Reionization Array

The Hydrogen Epoch of Reionization Array (HERA) is an array currently under construction in the Karoo reserve area in South Africa - following the conclusion of the PAPER experiment. HERA is built following the approach used for PAPER: a highly redundant array to maximize the sensitivity on a number of power spectrum modes measured using the avoidance approach. In order to increase the sensitivity with respect to PAPER, it employs 14 m diameter dishes that, in the final configuration, will be densely packed in a highly redundant hexagonal array configuration of ~ 350 m diameter. HERA is built with the purpose to provide a complete statistical characterization of cosmic reionization: its high brightness sensitivity configuration leads to a significant (> 10) power spectrum detection in the $0.2 < k < 0.4$ Mpc $^{-1}$ range throughout reionization (i.e., $6 \lesssim z \lesssim 12$; Pober et al., 2014; de Boer et al., 2017), fully constraining the evolution of the IGM neutral Hydrogen fraction. As the avoidance approach does not take advantage of foreground modeling, particular attention was paid to prevent the instrumental frequency response from corrupting intrinsically smooth foregrounds (Ewall-Wice et al., 2015; Patra et al., 2017). HERA is currently under construction, with more than 200 dishes deployed and science observations routinely carried out (Carilli et al. 2018, Kohn et al. 2019). New feeds that extend the sensitivity to the 50-250 MHz (i.e. enabling observations of the Cosmic Dawn) are currently deployed for testing. In summary, HERA is planned to deliver a complete characterization of cosmic reionization and to attempt the detection of the Cosmic Dawn. Given its redundant configuration, imaging capabilities remain limited and will be the target of a next generation experiment.

2.1.2 The Large aperture Experiment to detect the Dark Ages

The Large aperture Experiment to detect the Dark Ages (LEDA) is located in Owens Valley, California. It operates in the 30-88 MHz frequency range corresponding to $15 < z < 46$, therefore seeking to detect the 21 cm signal from the Cosmic Dawn. It is equipped to attempt the measurement of both the global signal via individual dipoles equipped with custom-built calibration sources and 21 cm fluctuations via an array of 256 dipoles. Dipoles are pseudo randomly distributed to achieve an essentially filled array within a 200 m diameter core, providing excellent imaging capabilities to Galactic diffuse emission - the brightest foreground component. The LEDA approach to measure the 21 cm signal can be versatile, allowing to image and subtract foregrounds but also to isolate them in the power spectrum domain without any specific modeling. Current simulations shows that if IGM heating occurs efficiently at $z \sim 16$, LEDA would be able to detect the 21 cm power spectrum at $k \sim 0.1 \text{ Mpc}^{-1}$ with a 10 signal to noise ratio in 3000 hours. First observations have set a 108 (mK)² upper limits on the 21 cm power spectrum at $k = 0.1 \text{ Mpc}^{-1}$ at $z = 18.4$ (Eastwood et al. 2019)

2.2 A Section

Lorem ipsum dolor sit amet, consectetur adipiscing elit. Duis eu egestas erat. Maecenas tincidunt lacinia tincidunt. Mauris id lectus nec neque feugiat condimentum vitae at diam. In vel orci nunc, non commodo mauris. Vivamus ipsum enim, vulputate quis pharetra non, molestie quis felis. Vivamus porttitor placerat turpis at accumsan. Nunc tortor velit, faucibus a rhoncus nec, blandit non elit. Nam consectetur lectus eu nisi blandit dapibus rhoncus dui tempus. Mauris fermentum dolor vel ipsum vulputate sit amet ultricies tortor lacinia. Donec ut nibh erat. Morbi nec mi ante. Integer nec vestibulum diam. Donec tincidunt pellentesque quam, ut interdum mauris venenatis condimentum. Nam condimentum, augue in aliquet gravida, neque dui elementum eros, id semper eros purus sed felis. Curabitur in justo sit amet sapien ultrices hendrerit at quis nibh. Quisque iaculis pulvinar tincidunt.

$$\begin{aligned}
 C(12) &= \left[\vec{\pi} \cdot \vec{\phi}(x+r) \right] \\
 &\approx 1 - \text{const} \frac{r^2}{L^2} \int_r^L \frac{xdx}{x^2} + \dots \\
 &\approx 1 - \text{const} \frac{r^2}{L^2} \ln \frac{xdx}{x^2} + \dots
 \end{aligned} \tag{2.1}$$

Aenean tellus risus, porta sit amet porta vitae, tincidunt ut felis. Class aptent taciti sociosqu ad litora torquent per conubia nostra, per inceptos himenaeos. Vestibulum ante ipsum primis in faucibus orci luctus et ultrices posuere cubilia Curae; Phasellus pulvinar placerat velit auctor egestas. Vivamus euismod fringilla tincidunt. Sed ut magna felis, id sollicitudin nunc. Quisque a dui eu erat consectetur egestas a quis justo. Aenean euismod congue diam, vel posuere urna fermentum sit amet. Lorem ipsum dolor sit amet, consectetur adipiscing elit. Mauris faucibus lacus eget est mollis auctor. Donec at nibh ligula, et posuere massa. Phasellus quis leo diam [1]. Donec aliquam blandit risus, eu venenatis ante euismod eu. Curabitur cursus justo id arcu condimentum feugiat. Integer sapien urna, vulputate et adipiscing nec, convallis et justo. Suspendisse in ipsum at felis ornare interdum [2],

[illegible]

Table 2.1: Greek Letters.

α	β	γ	δ	ε	ζ	η
θ	ϑ	γ	κ	λ	μ	ξ
o	π	$\overline{\omega}$	ρ	ρ	σ	ς
τ	υ	ϕ	φ	χ	ψ	ω
Γ	Δ	Θ	Λ	Ξ	Π	Σ
Φ	Ψ	Ω				

Cras adipiscing sagittis nunc vel luctus. Suspendisse volutpat augue quis erat semper consequat dignissim tellus euismod. Morbi hendrerit, tellus id aliquam iaculis, nibh leo tincidunt eros, vitae varius ligula felis in mi.

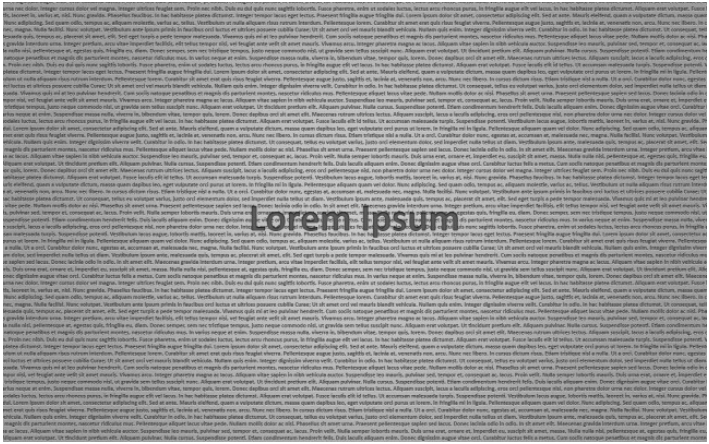


Figure 2.2: This is figure 2 in chapter 1.

Bibliography

- [1] KI Diamantaras and SY Kung. *Principal component neural networks: theory and applications*. John Wiley & Sons, Inc. New York, NY, USA, 1996.
- [2] D. Tulone and S. Madden. PAQ: Time Series Forecasting for Approximate Query Answering in Sensor Networks. In *Proceedings of the 3rd European Workshop on Wireless Sensor Networks*, pages 21–37. Springer, 2006.